Colloidal Antimony Sulfide Nanoparticles as a High-Performance Anode Material for Li-ion and Na-ion Batteries

SCIENTIFIC REPORTS
nature research

OPEN

Colloidal Antimony Sulfide Nanoparticles as a High-Performance Anode Material for Li-ion and Na-ion Batteries

Kostiantyn V. Kravchyk[1,2*], Maksym V. Kovalenko[1,2] & Maryna I. Bodnarchuk[1*]

To maximize the anodic charge storage capacity of Li-ion and Na-ion batteries (LIBs and SIBs, respectively), the conversion–alloying-type Sb_2S_3 anode has attracted considerable interest because of its merits of a high theoretical capacity of 946 mAh g^{-1} and a suitable anodic lithiation/delithiation voltage window of 0.1–2 V *vs*. Li^+/Li. Recent advances in nanostructuring of the Sb_2S_3 anode provide an effective way of mitigating the challenges of structure conversion and volume expansion upon lithiation/sodiation that severely hinder the Sb_2S_3 cycling stability. In this context, we report uniformly sized colloidal Sb_2S_3 nanoparticles (NPs) as a model Sb_2S_3 anode material for LIBs and SIBs to investigate the effect of the primary particle size on the electrochemical performance of the Sb_2S_3 anode. We found that compared with microcrystalline Sb_2S_3, smaller *ca*. 20–25 nm and *ca*. 180–200 nm Sb_2S_3 NPs exhibit enhanced cycling stability as anode materials in both rechargeable LIBs and SIBs. Importantly, for the *ca*. 20–25 nm Sb_2S_3 NPs, a high initial Li-ion storage capacity of 742 mAh g^{-1} was achieved at a current density of 2.4 A g^{-1}. At least 55% of this capacity was retained after 1200 cycles, which is among the most stable performance Sb_2S_3 anodes for LIBs.

Lithium-ion batteries (LIBs) are the most well-known rechargeable electrochemical energy storage devices, and they are a key component of electric mobility and portable electronics[1–4]. Sodium-ion batteries (SIBs) are conceptually similar, and they have attracted enormous attention in recent years because of the higher natural abundance of sodium and more favorable distribution of sodium reserves compared with lithium[5–13]. Although graphite is currently the main commercialized anode material for LIBs, its low theoretical charge storage capacity (372 mAh g^{-1}) limits its application in new generation batteries, requiring exploration of new electrode materials with higher capacity and stable cycling performance[14]. With respect to SIBs, the search for efficient Na-storing anodes is a high priority, because graphite shows low Na-ion capacities of 30–35 mAh g^{-1}[15], while other carbonaceous materials have low tap densities and exhibit capacities of less than 300 mAh g^{-1}[16]. Additionally, the relatively low potential of carbon sodiation (~0 V *vs*. Na^+/Na) leads to deposition of sodium metal on the carbon electrode surfaces, which may eventually result in compromised safety[17].

Over the past decade, much attention has been focused on development of alternative anode materials for both LIBs and SIBs[12]. In particular, low-cost and environmentally benign Sb_2S_3 anodes have attracted great interest because of their high capacities and relatively low redox lithiation/sodiation potentials[18–45]. Theoretically, Sb_2S_3 can generate a specific capacity as high as 946 mAh g^{-1} through conversion and alloying reactions (corresponding to 12 mol of lithium/sodium and electrons per formula unit). However, harnessing this storage potential of Sb_2S_3 is hindered by its poor capacity retention owing to the structural (conversion) and volume (alloying) changes during discharging/charging, which lead to mechanical disintegration of the electrodes and thus loss of electrical connectivity. These difficulties can be mitigated by nanostructuring, particularly when the active material is embedded in an elastic and conductive network that helps to enhance electronic transport and reduce the cycling instability caused by volumetric changes in the conversion–alloying-type anode material[36,46,47]. Specifically, in the last few years, extensive effort has focused on various forms of nanostructured Sb_2S_3, such as

[1]Laboratory for Thin Films and Photovoltaics, Empa – Swiss Federal Laboratories for Materials Science and Technology, Überlandstrasse 129, CH-8600, Dübendorf, Switzerland. [2]Laboratory of Inorganic Chemistry, Department of Chemistry and Applied Biosciences, ETH Zürich, Vladimir-Prelog-Weg 1, CH-8093, Zürich, Switzerland. *email: kravchyk@inorg.chem.ethz.ch; maryna.bodnarchuk@empa.ch

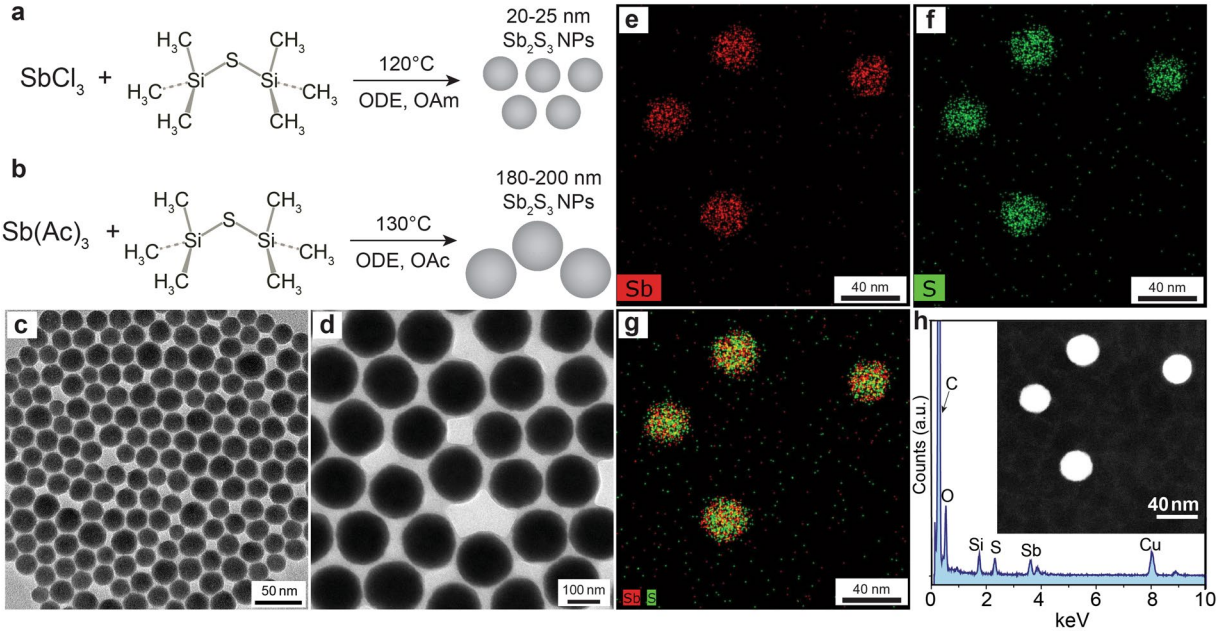

Figure 1. Schematics of one-pot synthesis of the (**a**) *ca*. 20–25 nm and (**b**) 180–200 nm Sb_2S_3 NPs. TEM images of the (**c**) *ca*. 20–25 nm and (**d**) *ca*. 180–200 nm Sb_2S_3 NPs. (**e**) Sb-Lα and (**f**) S-Kα elemental STEM-EDXS maps of the *ca*. 20–25 nm Sb_2S_3 NPs. (**g**) Reconstructed overlay image of the elemental maps shown in (**e**) and (**f**). (**h**) EDXS spectrum of the small Sb_2S_3 NPs. The insert shows a high-angle annular dark-field scanning transmission electron microscopy image of the *ca*. 20–25 nm Sb_2S_3 NPs.

Sb_2S_3 nanowires[24,48–51], nanorods[45,52,53], nanoparticles (NPs)[37,54–57], nanocables[58], and Sb_2S_3/C nanocomposites[23], to maximize the anodic charge-storage capacity and improve the cycling performance. Notably, the electrochemical performance of highly uniform colloidal Sb_2S_3 NPs has not been reported. Such NPs are an ideal platform for studying the effects of the size and electrode morphology on the charge storage capacity and cycling stability of Sb_2S_3 anodes.

In this study, we synthesized uniformly sized colloidal Sb_2S_3 NPs whose size is tunable in 10–200 nm size range, which allowed us to comprehensively investigate the effect of the primary particle size on the electrochemical behaviour of Sb_2S_3 as the anode material for LIBs and SIBs. We assessed the pros and cons of nano-Sb_2S_3 anodes in comparison with commercial microcrystalline Sb_2S_3 (hereafter denoted bulk Sb_2S_3, Figure S1). We note that although synthesis of Sb_2S_3 NPs might be prohibitively expensive for practical application in commercial batteries, the insight gained from using such precisely tunable model NPs can guide development of Sb_2S_3 anodes for both LIBs and SIBs. We found that at current rates of 0.3–12 A g^{-1}, the Li-ion storage capacities for anodes composed of both *ca*. 20–25 nm (1055–608 mAh g^{-1}) and *ca*. 180–200 nm Sb_2S_3 (970–574 mAh g^{-1}) were significantly higher than for their bulk counterpart (683–418 mAh g^{-1}). For Na-ion storage, the capacities of nano-Sb_2S_3 and bulk Sb_2S_3 anodes were similar. Regarding the cycling stability, the major finding was that nano-Sb_2S_3 exhibited significantly higher capacity retention for both Li-ion and Na-ion storage than bulk Sb_2S_3. Notably, unprecedented Li-ion capacity retention of 55% was achieved for *ca*. 20–25 nm Sb_2S_3 NPs at a current density of 2.4 A g^{-1} after 1200 cycles.

Results and Discussion

The general synthetic route for preparation of *ca*. 20–25 nm amorphous antimony sulfide NPs using octadecene (ODE) as a solvent in the presence of oleylamine (OAm) as a surface capping ligand is shown in Fig. 1a. In a typical synthesis, the Sb_2S_3 NPs were synthesized by the hot-injection technique using antimony(III) chloride and bis(trimethylsilyl)sulfide ($(TMS)_2S$) as the antimony and sulfur precursors, respectively. After injection of $(TMS)_2S$ into the $SbCl_3$/ODE mixture, the color of the reaction solution rapidly changed to red-orange. The reaction temperature was maintained at 120 °C for 15 min. Transmission electron microscopy (TEM) and X-ray diffraction (XRD) analysis confirmed formation of amorphous spherical *ca*. 20–25 nm antimony sulfide NPs with a narrow size distribution (Figs. 1c and S2a). A longer reaction time of 30 min resulted in formation of *ca*. 1.5–2.0 μm long crystalline Sb_2S_3 nanorods with diameters of *ca*. 150–200 nm (Figure S3). When the $(TMS)_2S$ solution was injected at 100 °C and maintained at this temperature for 15 min, *ca*. 8–10 nm amorphous Sb_2S_3 NPs were obtained (Figure S4). Scanning transmission electron microscopy with energy-dispersive X-ray spectroscopy (STEM-EDXS) measurements of the as-synthesized *ca*. 20–25 nm Sb_2S_3 NPs revealed that Sb and S were homogeneously distributed throughout each NP (Fig. 1e,f, g, h). From scanning electron microscopy with energy-dispersive X-ray spectroscopy (SEM-EDXS) analysis, the atomic ratio of Sb, S and O was about 1:1.4:0.1 (Figure S5). The presence of detectable oxygen in the EDS spectrum could be because of oxidation of the NPs during synthesis, cleaning, or preparation of the specimen. Notably, similar synthesis of Sb_2S_3 NPs was reported

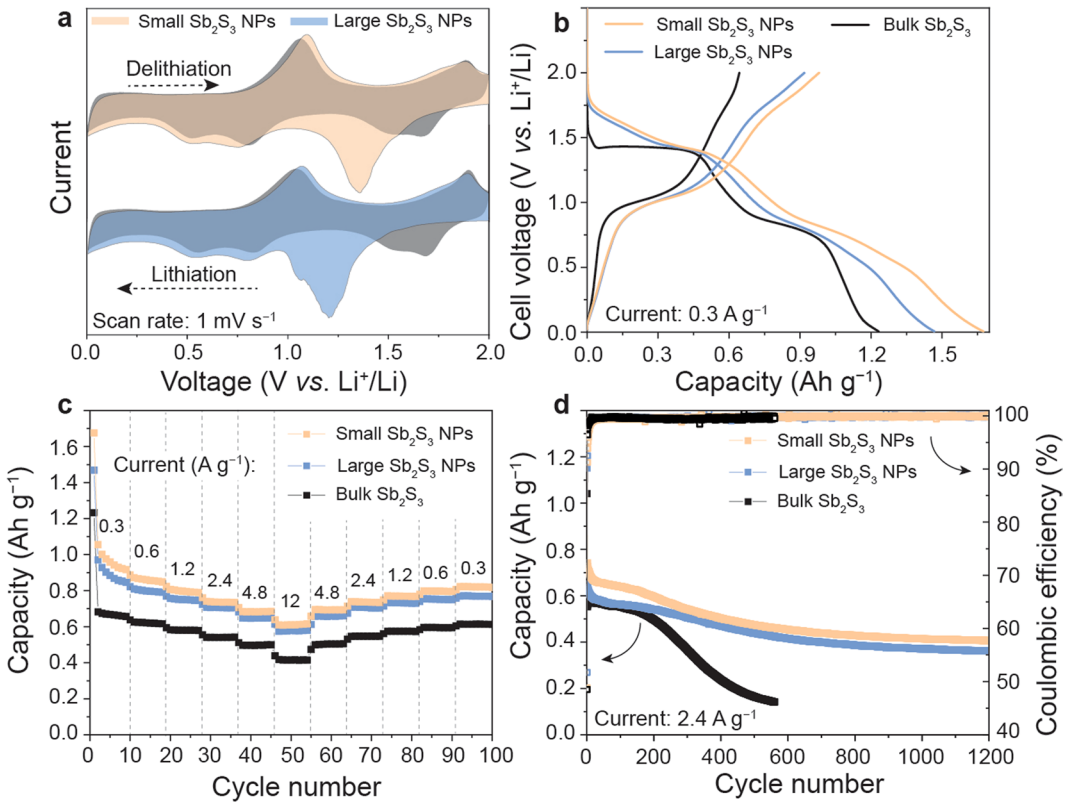

Figure 2. Electrochemical results of the Sb_2S_3 electrodes cycled with lithium electrolyte (1 M $LiPF_6$ in ethylene carbonate/dimethyl carbonates (EC/DMC)) in a half-cell configuration using metallic lithium as the counter and reference electrode. (**a**) CV curves (the first cycle is shown in orange or blue and the second cycle is shown in grey) of the small and large Sb_2S_3 NPs measured at a scan rate of 1 mV s^{-1} (see Figure S8 for details). (**b**) Galvanostatic charge–discharge curves of the small Sb_2S_3 NPs, large Sb_2S_3 NPs, and bulk Sb_2S_3 during the first cycle. (**c**) Rate capacity and (**d**) cycling stability measurements of Li-ion half-cells using Sb_2S_3 anodes made from small Sb_2S_3 NPs, large Sb_2S_3 NPs, and bulk Sb_2S_3. The corresponding galvanostatic charge–discharge curves and Coulombic efficiency measured at current densities of 0.3–12 A g^{-1} and different cycle number are shown in Figures S9, S10 and S11 respectively.

by Bakr *et al.*[59]. using $SbCl_3$ and $(TMS)_2S$ in ODE with oleic acid (OAc) as a ligand. The synthesis yielded relatively polydisperse *ca.* 30–50 nm Sb_2S_3 NPs with a chain-like structure. In our synthesis, the use of the OAm ligand resulted in slower reaction kinetics, causing more homogenous nucleation and growth of Sb_2S_3 NPs in comparison with the OAc ligand.

Larger Sb_2S_3 NPs of approximately *ca.* 180–200 nm were synthesized in a similar way to the *ca.* 20–25 nm Sb_2S_3 NPs by replacing the antimony(III) chloride precursor and OAm ligand with antimony acetate and OAc, respectively (Figs. 1b,d and S2b, S6; for details see the experimental section). By changing of the $(TMS)_2S$ sulfur source to S/OAm (elemental sulfur dissolved in OAm), crystalline Sb_2S_3 nanoplates were obtained (Figure S7).

The galvanostatic cycling measurements of the Sb_2S_3 NPs are summarized in Figs. 2 and 3. For electrochemical testing, the Sb_2S_3 NPs were treated with a 1 M solution of hydrazine in acetonitrile for 2 h[60,61]. The untreated NPs gave no operational electrodes because of the isolating long-chain capping molecules surrounding the as-synthesized Sb_2S_3 NPs. In addition to the effect of the active material, the charge storage capacity of the electrode strongly depends on the electrode formulation (the origin and amounts of the binder and conductive additive), electrode thickness, porosity, temperature, electrolyte, and so forth. Therefore, with the aim of distinguishing the size effect from the other factors, the following experimental parameters were fixed for all of the electrodes: (i) the choice and mass fractions of the binder and carbon black and (ii) the electrolyte composition. All of the electrodes contained 64 wt% of the active material, 15 wt% carboxymethylcellulose as a binder, and 21 wt% carbon black as a conductive additive. The electrochemical tests were performed in Li-ion or Na-ion half-cells with elemental lithium or sodium acting as both the counter and reference electrodes, respectively. Further details of electrode preparation and assembly of the batteries are given in the Supporting Information.

The cyclic voltammetry (CV) curves of electrodes composed of *ca.* 20–25 nm and *ca.* 180–200 nm Sb_2S_3 NPs (hereafter denoted small and large Sb_2S_3 NPs, respectively) measured in Li-ion electrolyte at a scan rate of 1 mV s^{-1} are shown in Fig. 2a. In the first cathodic cycle, the broad peak at about 1.2–1.4 V *vs.* Li^+/Li can be attributed to formation of a solid electrolyte interphase (SEI) layer and the conversion reaction of Sb_2S_3 NPs ($Sb_2S_3 + 6Li^+ + 6e^- \rightarrow 2Sb + 3Li_2S$). Upon further lithiation, two reduction peaks at 0.7 and 0.5 V *vs.* Li^+/Li appeared, which are ascribed to formation of Li_2Sb and Li_3Sb alloys, respectively. In the reverse scan, the Sb_2S_3 electrode

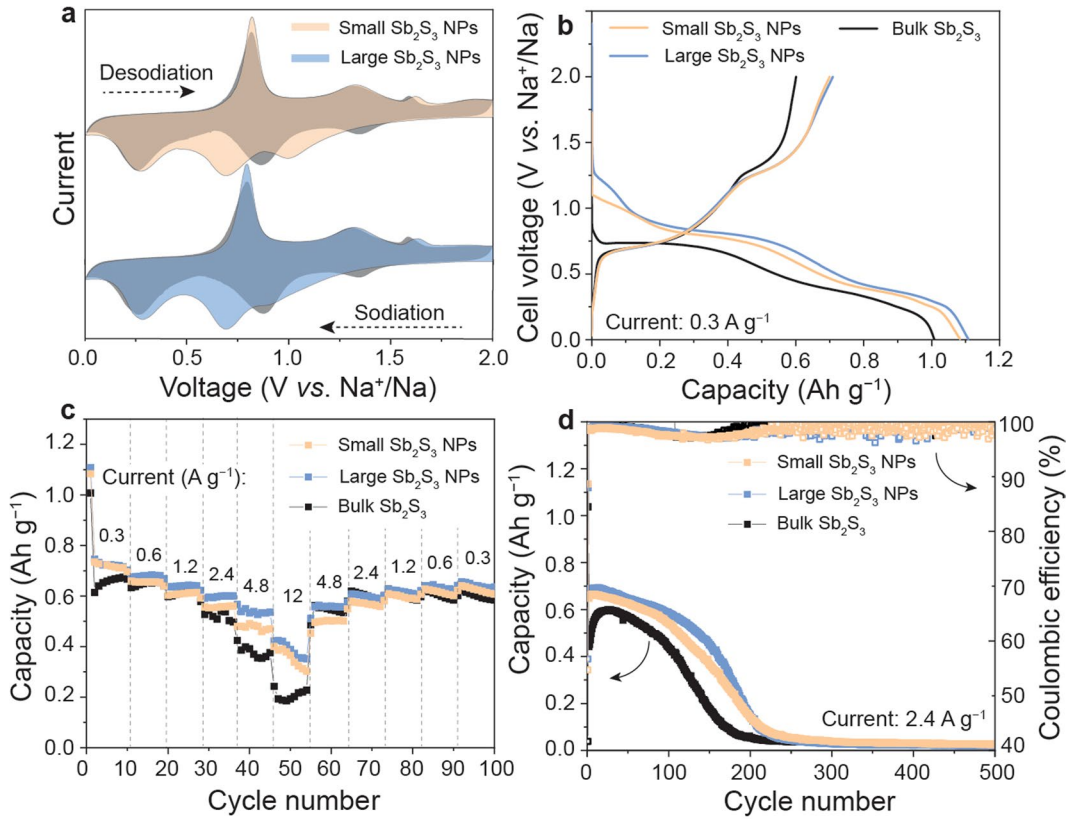

Figure 3. Electrochemical results of the Sb_2S_3 electrodes cycled with sodium electrolyte (1 M $NaClO_4$ in PC) in a half-cell configuration using metallic sodium as the counter and reference electrode. (**a**) CV curves (the first cycle is shown in orange or blue and the second cycle is shown in grey) of the electrodes composed of small and large Sb_2S_3 NPs measured at a scan rate of 1 mV s^{-1} (see Figure S12 for details). (**b**) Galvanostatic charge–discharge curves of the electrodes composed of small Sb_2S_3 NPs, large Sb_2S_3 NPs and bulk Sb_2S_3 during the first cycle. (**c**) Rate capacity and (**d**) cycling stability of Na-ion half-cells using Sb_2S_3 anodes composed of small Sb_2S_3 NPs, large Sb_2S_3 NPs, and bulk Sb_2S_3. The corresponding galvanostatic charge–discharge curves and Coulombic efficiency measured at current densities of 0.3–12 A g^{-1} and different cycle numbers are shown in Figures S13, S14 and S15, respectively.

showed two peaks at 1 and 1.9 V, which are associated with delithiation of the Li_3Sb alloy phase following formation of Sb_2S_3. The discharge voltage profiles of the Sb_2S_3 NPs are shown in Fig. 2b. The profiles of the Sb_2S_3 NPs are similar to the CV curves, showing two-step reduction of Sb_2S_3 eventually resulting in formation of metallic Sb (conversion reaction, voltage range 1.7–1.2 V *vs.* Li^+/Li) and the Li_3Sb alloy (alloying reaction, voltage range 0.4–1.0 V *vs.* Li^+/Li). As follows from CV measurements, alloying of Sb in bulk Sb_2S_3, large and small Sb_2S_3 NPs takes place differently. In the bulk system, it appears that the lithiation proceeds through the direct formation of Li_3Sb alloy. On the contrary, in the case of Sb_2S_3 NPs, the lithiation takes place through sequential formation of Li_2Sb and Li_3Sb alloys, respectively.

The Li-ion discharge capacities of Sb_2S_3 anodes composed of small Sb_2S_3 NPs, large Sb_2S_3 NPs, and microcrystalline Sb_2S_3 at charge/discharge current densities of 0.3–12 A g^{-1} are shown in Fig. 2c. At a low current density of 0.3 A g^{-1}, the anodes composed of small and large Sb_2S_3 NPs exhibited theoretical capacities of about 1000 mAh g^{-1} with Coulombic efficiency of 97%–98% (Figure S10). The capacity retention values of the Sb_2S_3 anodes composed of small and large Sb_2S_3 NPs were 60% and 61% at 12 A g^{-1}, respectively. The slightly higher discharge capacity of the anode composed of small Sb_2S_3 NPs during the first few cycles at a low current density of 0.3 A g^{-1} can be attributed to formation and stabilization of a SEI layer. For the bulk Sb_2S_3 system, the anode composed of microparticles of Sb_2S_3 exhibited only 60% of the theoretical capacity at 0.3 A g^{-1}, but it retained 57% of its initial charge-storage capacity at high current density, similar to the Sb_2S_3 NP anodes. Regarding the cycling performance, the Sb_2S_3 NP and bulk Sb_2S_3 anodes showed stable capacities for the first 200 cycles (Fig. 2d). However, upon prolonged cycling, the capacity of the bulk Sb_2S_3 anode gradually decreased.

The capacities of the anodes composed of small and large Sb_2S_3 NPs were stable for 1200 cycles. The anode composed of small Sb_2S_3 NPs systematically showed at least 5% higher capacity than the anode composed of large NPs. In all cases, the Coulombic efficiency was relatively low for the initial 10–20 cycles (95%–97%), but it then increased to more than 99% upon cycling. As mentioned above, the higher cycling stability of the anode composed of Sb_2S_3 NPs compared with that composed of bulk Sb_2S_3 probably originates from the lower kinetic constraints of nanomaterials for conversion and alloying reactions. For instance, for alloying anode materials

(e.g., Sn, Si, and Ge), several studies have demonstrated the existence of a critical size of the particles below which they do not fracture[62,63]. Furthermore, we speculate that the amorphicity of the Sb_2S_3 NPs aids in isotropic expansion/contraction upon their lithiation/delithiation, eventually resulting in reduction of the amount of anisotropic mechanical stress within the electrode.

In Na-ion cells with Sb_2S_3 NP electrodes, CV measurements showed three peaks at *ca*. 1, 0.7, and 0.27 V associated with formation of a SEI layer/intercalation of sodium ions into Sb_2S_3, conversion, and alloying reactions, respectively (Fig. 3a, see Figure S12 for details). Upon desodiation (reverse scan), the Sb_2S_3 electrode showed two peaks at 0.8 and 1.3 V *vs*. Na^+/Na, which are associated with dealloying of Sb and reconversion of the Sb_2S_3 phase. The third peak at a higher potential of 1.6 V can be assigned to deinsertion of Na^+ ions from Sb_2S_3. In general, the CV curves (Fig. 3a) and shape of the voltage profiles (Fig. 3b) suggest conversion and the alloying mechanism of sodiation of the Sb_2S_3 NPs in the voltage ranges 0.6–1 V and 0.1–0.5 V *vs*. Na^+/Na, respectively.

In Na-ion cells, the nano-Sb_2S_3 and bulk Sb_2S_3 electrodes showed similar charge storage capacities of ~580–620 mAh g^{-1} at current densities of 0.3–1.2 A g^{-1} (Fig. 3c). The similar capacities of the nano-Sb_2S_3 and bulk Sb_2S_3 anodes in Na-ion cells can be explained by the presence of an amorphous surface oxide shell on the Sb_2S_3 NPs (see Figures S5 and S6 for EDS spectra). This leads to formation of Na_2O, eventually resulting in irreversible capacity loss in the first discharge cycle. The much smaller differences among the capacities of the electrodes composed of small Sb_2S_3 NPs, large Sb_2S_3 NPs, and bulk Sb_2S_3 for Na-ion cells than Li-ion cells can be explained by the different properties of Li_2O and Na_2O. We suspect that Li_2O acts as a relatively benign impurity covering the Sb_2S_3 NPs because of its high Li-ion conductivity. In contrast, Na_2O is a much poorer Na^+ conductor, leading to exclusion of some Sb_2S_3 NPs from the reversible charge/discharge storage capacity. The results of stability tests for 500 cycles at a high current density of 2.4 A g^{-1} are shown in Fig. 3d. In general, the charge storage capacities were consistently higher for nano-Sb_2S_3 than bulk Sb_2S_3, although the capacities remained stable for only about 50 and 100 cycles for bulk Sb_2S_3 and nano-Sb_2S_3, respectively.

Conclusions

In summary, we have reported facile colloidal synthesis of highly uniform colloidal Sb_2S_3 NPs with mean particle sizes in the ranges *ca*. 20–25 nm and *ca*. 180–200 nm. The underlying chemistry is based on the reaction of antimony(III) chloride/acetate and $(TMS)_2S$ in ODE using OAm/OAc as a coordinating ligand at high temperature of 120/130 °C for small/large Sb_2S_3 NPs. Both the small and large Sb_2S_3 NPs showed electrochemical cyclic stability superior to that of bulk Sb_2S_3 in both LIBs and NIBs. In particular, the small NPs exhibited high retention of the capacity upon extended cycling, losing only 55% of their initial capacity over 1200 cycles at a high density of 2.4 A g^{-1}.

Methods

Chemicals. Oleic acid (OAc, Sigma-Aldrich), oleylamine (OAm, Acros, 80–90%), octadecene (Sigma-Aldrich), octadecene (ODE, Sigma-Aldrich), antimony (III) chloride (ABCR), antimony (III) acetate (Sigma-Aldrich), bis[trimethylsilyl]sulfide (Sigma-Aldrich), chloroform and acetone were used as received.

Synthesis of ~20–25 nm spherical amorphous NPs. In a typical synthesis 0.5 mL oleylamine, OAm, (Acros, 80–90%) and 4 mL octadecene (ODE) were loaded into 25-mL flask and dried at 100 °C for 30 min. Then, 114 mg (0.5 mmol) $SbCl_3$ were added to the flask under argon. The reaction mixture was heated up to 120 °C and 0.5 mmol bis[trimethylsilyl]sulfide (100 μL, $(TMS)_2S$) in 2 mL dried ODE was then injected into the reaction flask. The color of the solution has changed to red-orange. In 15 min reaction mixture was cool down to room temperature and washed 2 times by chloroform/acetone and separated by centrifugation. After second washing step, Sb_2S_3 NPs were re-dispersed in oleic acid (OAc)/chloroform mixture (50 μL OAc in 2–3 mL chloroform) and stored under ambient condition. Injection of $(TMS)_2S$ solution at 100 °C and maintaining this temperature through the reaction for 15 min leads to formation of 8–10 nm amorphous Sb_2S_3 NPs. Injection of $(TMS)_2S$ solution at 170–180 °C and maintaining this temperature through the reaction for 3–5 min leads to formation of micrometer-sized crystalline rods (Figure S3a). Powder XRD of as-prepared NRs shows that they are highly crystalline and their XRD pattern corresponds to stibnite phase of antimony sulfide (Figure S3b). Crystalline rods could be also obtained at 120 °C in case of longer growth time. In 30 min after injection of $(TMS)_2S$ the orange color of the reaction mixture started to change into a gray-black.

Synthesis of ~180–200 nm spherical amorphous NPs. In a typical synthesis, 2.5 mL OAc, 2.5 mL ODE and 0.5 mmol antimony (III) acetate were loaded into 25-mL flask and dried at 100 °C for 30 min. The reaction mixture was heated up to 130 °C under argon. At 130 °C, 0.375 mmol $(TMS)_2S$ (78 μL) in 2.5 mL dried ODE was then injected into the reaction flask. The color of the solution has changed to orange. In 3–5 min, reaction mixture was cool down to room temperature and final product was washed 2 times by chloroform/acetone and separated by centrifugation. After washing Sb_2S_3 NPs were re-dispersed in OAc/chloroform mixture (50 μL OAc in 2–3 mL chloroform) and stored under ambient condition.

Synthesis of thin crystalline Sb_2S_3 nanoplatelets. We have found that another sulfur source such as elemental sulfur in OAm effects on the morphology of Sb_2S_3 NPs yielding the formation of thin crystalline Sb_2S_3 nanoplatelets (Figure S7a). Their average size is approximately several hundred nanometers and their XRD pattern suggest that they are highly crystalline (Figure S7b). In a typical synthesis, 5 mL OAm (Acros) and 0.25 mmol (57 mg) antimony (III) chloride were loaded into 25-mL flask and dried at 80 °C for 30 min. The reaction mixture was heated up to 110 °C under argon. At 110 °C, 1 mmol (32 mg) sulfur dissolved in 2 mL OAm (Acros) was then injected into the reaction flask. Then temperature of reaction mixture was increased to 180 °C and kept for 15 min. The final product was washed 2 times by chloroform/acetone and separated by centrifugation. Sb_2S_3 nanoplatelets

were re-dispersed in OAc/chloroform mixture (50 μL OAc in 2–3 mL chloroform) and stored under ambient condition.

Battery components. Carbon black (Super C65, TIMCAL), carboxymethyl cellulose (CMC, Grade: 2200, Lot No. B1118282, Daicel Fine Chem Ltd.), $NaClO_4$ (98%, Alfa Aesar, additionally dried), propylene carbonate (BASF, battery grade), 4-fluoro-1,3-dioxolan-2-one (FEC, Hisunny Chemical, battery grade), 1 M solution of $LiPF_6$ in ethylene carbonate/dimethyl carbonate (EC/DMC, Novolyte, Celgard separator (Celgard 2400, 25 μm microporous monolayer polypropylene membrane, Celgard Inc. USA), glass microfiber separator (GF/D, Cat No. 1823–257, Whatman), Al foil (MTI Corporation), Na foil (Sigma-Aldrich), Li foil (MTI Corp.), Sb_2S_3 (99.995%, Sigma Aldrich), Coin-type cells (Hohsen Corp., Japan),

Electrochemical characterization of antimony sulfide. Coin-type cells were assembled in an argon-filled glove box ($O_2 < 1$ ppm, $H_2O < 1$ ppm) using one layer separator (glass fiber) for NIBs and two layers of separators (Celgard and glass fiber) for LIBs. Elemental sodium or lithium served as both reference and counter electrodes. As electrolyte 1 M $NaClO_4$ in PC was used for Na-ion batteries and 1 M $LiPF_6$ in EC:DMC (1:1 by wt.) for Li-ion batteries. To improve cycling stability 3% of FEC were added to both electrolytes. Electrochemical measurements were performed using constant current mode for both, charge and discharge steps between 0.01–2.5 V for both Na and Li-ion batteries on a MPG2 multi-channel workstation (Bio-Logic).

Materials characterization. TEM samples were prepared by dropping a solution of Sb_2S_3 NPs onto standard amorphous carbon-coated TEM grids. TEM images were recorded using JEOL JEM-2200FS microscope operated at 200 kV, STEM images and EDXS spectrum were collected on FEI Talos F200X operated at 200 kV and equipped with Super-X EDS system (4 detector configuration). Scanning electron microscopy (SEM) measurements were done on a Quanta 200 F microscope (Thermo Fisher Scientific) operated at an acceleration voltage Vacc = 20 kV. Energy-dispersive X-ray spectroscopy (EDXS) was performed with an Octane SDD detector (EDAX (Ametec)) attached to the microscope column. Powder X-ray diffraction pattern was collected with STOE STADIP powder diffractometer.

Received: 30 November 2019; Accepted: 29 January 2020;
Published online: 13 February 2020

References

1. Armand, M. & Tarascon, J. M. Building Better Batteries. *Nat.* **451**, 652 (2008).
2. Palacín, M. R. Recent Advances in Rechargeable Battery Materials: a Chemist's Perspective. *Chem. Soc. Rev.* **38**, 2565–2575 (2009).
3. Goodenough, J. B. Energy Storage Materials: A Perspective. *Energy Storage Mater.* **1**, 158–161 (2015).
4. Walter M., Kovalenko M.V., Kravchyk K.V. Challenges and Benefits of Post-Lithium-Ion Batteries. *New J Chem*, (2020).
5. Palomares, V. *et al*. Na-Ion Batteries, Recent Advances and Present Challenges to Become Low Cost Energy Storage Systems. *Energy Env. Sci.* **5**, 5884–5901 (2012).
6. Dahbi, M., Yabuuchi, N., Kubota, K., Tokiwa, K. & Komaba, S. Negative Electrodes for Na-Ion Batteries. *Phys. Chem. Chem Phys* **16**, 15007–15028 (2014).
7. Yabuuchi, N., Kubota, K., Dahbi, M. & Komaba, S. Research Development on Sodium-Ion Batteries. *Chem. Rev.* **114**, 11636–11682 (2014).
8. Luo, W. *et al*. Na-Ion Battery Anodes: Materials and Electrochemistry. *Acc. Chem. Res.* **49**, 231–240 (2016).
9. Slater, M. D., Kim, D., Lee, E. & Johnson, C. S. Sodium-Ion Batteries. *Adv. Funct. Mater.* **23**, 947–958 (2013).
10. Palomares, V., Casas-Cabanas, M., Castillo-Martínez, E., Han, M. H. & Rojo, T. Update on Na-Based Battery Materials. A Growing Research Path. *Energy Env. Sci.* **6**, 2312–2337 (2013).
11. Kim, S.-W., Seo, D.-H., Ma, X., Ceder, G. & Kang, K. Electrode Materials for Rechargeable Sodium-Ion Batteries: Potential Alternatives to Current Lithium-Ion Batteries. *Adv. Energy Mater.* **2**, 710–721 (2012).
12. Liu, J. *et al*. SnP Nanocrystals as Anode Materials for Na-Ion Batteries. *J. Mater. Chem. A* **6**, 10958–10966 (2018).
13. Kravchyk, K. V., Zünd, T., Wörle, M., Kovalenko, M. V. & Bodnarchuk, M. I. $NaFeF_3$ Nanoplates as Low-Cost Sodium and Lithium Cathode Materials for Stationary Energy Storage. *Chem. Mater.* **30**, 1825–1829 (2018).
14. Larcher, D. & Tarascon, J. M. Towards Greener and More Sustainable Batteries for Electrical Energy Storage. *Nat. Chem.* **7**, 19 (2014).
15. Ge, P. & Fouletier, M. Electrochemical Intercalation of Sodium in Graphite. *Solid. State Ion.* **28-30**, 1172–1175 (1988).
16. Alcántara, R., Jiménez-Mateos, J. M., Lavela, P. & Tirado, J. L. Carbon Black: a Promising Electrode Material for Sodium-Ion Batteries. *Electrochem. Commun.* **3**, 639–642 (2001).
17. Xiao, B., Rojo, T. & Li, X. Hard Carbon as Sodium-Ion Battery Anodes: Progress and Challenges. *ChemSusChem* **12**, 133–144 (2019).
18. Wen, S., Zhao, J., Zhao, Y., Xu, T. & Xu, J. Reduced Graphene Oxide (RGO) Decorated Sb_2S_3 Nanorods as Anode Material for Sodium-Ion Batteries. *Chem. Phys. Lett.* **716**, 171–176 (2019).
19. Tian, Y. *et al*. Facile Spray Drying Approach to Synthesize Sb_2Se_3/rGO Composite Anode for Lithium-Ion Battery. *J. Nanopart. Res.* **21**, 15 (2019).
20. Shi, Y. *et al*. Sb_2S_3@PPy Coaxial Nanorods: A Versatile and Robust Host Material for Reversible Storage of Alkali Metal Ions. *Nanomaterials* **9**, 560 (2019).
21. Mullaivananathan, V. & Kalaiselvi, N. Sb_2S_3 Added Bio-Carbon: Demonstration of Potential Anode in Lithium and Sodium-Ion Batteries. *Carbon* **144**, 772–780 (2019).
22. Man, Q., Hou, Q., Liu, P., Jin, R. & Li, G. Cube-Like Sb_2Se_3/C Constructed by Ultrathin Nanosheets as Anode Material for Lithium and Sodium-Ion Batteries. *Ion.* **25**, 1551–1558 (2019).
23. Liu, Y. *et al*. Plasma Milling Modified Sb_2S_3-graphite Nanocomposite as a Highly Reversible Alloying-Conversion Anode Material for Lithium Storage. *Electrochim. Acta* **310**, 26–37 (2019).
24. Dong, Y. *et al*. Nitrogen-Doped Carbon-Encapsulated Antimony Sulfide Nanowires Enable High Rate Capability and Cyclic Stability for Sodium-Ion. *Batteries. ACS Appl. Nano Mater.* **2**, 1457–1465 (2019).
25. Deng, M. *et al*. Natural Stibnite Ore (Sb_2S_3) Embedded in Sulfur-Doped Carbon Sheets: Enhanced Electrochemical Properties as Anode for Sodium Ions Storage. *RSC Adv.* **9**, 15210–15216 (2019).
26. Dai, S. *et al*. Design Strategies in Metal Chalcogenides Anode Materials for High-Performance Sodium-Ion Battery. *Mater. Today Energy* **12**, 114–128 (2019).
27. Zheng, T., Li, G., Zhao, L. & Shen, Y. Flowerlike Sb_2S_3/PPy Microspheres Used as Anode Material for High-Performance Sodium-Ion Batteries. *Eur. J. Inorg. Chem.* **2018**, 1224–1228 (2018).

28. Yao S., *et al*. Ultrathin Sb_2S_3 Nanosheet Anodes for Exceptional Pseudocapacitive Contribution to Multi-Battery Charge Storage. *Energy Storage Mater*, (2018).
29. Luo, W. *et al*. Imbedding Ultrafine Sb_2S_3 Nanoparticles in Mesoporous Carbon Sphere for High-Performance Lithium-Ion Battery. *Electrochim. Acta* **290**, 185–192 (2018).
30. Fang, Y., Yu, X.-Y. & Lou, X. W. Formation of Polypyrrole-Coated Sb_2Se_3 Microclips with Enhanced Sodium-Storage Properties. *Angew. Chem, Int. Ed.* **57**, 9859–9863 (2018).
31. Dong, Y., Yang, S., Zhang, Z., Lee, J.-M. & Zapien, J. A. Enhanced electrochemical performance of lithium ion batteries using Sb_2S_3 nanorods wrapped in graphene nanosheets as anode materials. *Nanoscale* **10**, 3159–3165 (2018).
32. Ru, Q. *et al*. Biological Carbon Skeleton of Lotus-Pollen Surrounded by Rod-Like Sb_2S_3 as Anode Material in Lithium Ion Battery. *Mater. Lett.* **198**, 57–60 (2017).
33. Zhu, Y. *et al*. High Rate Capability and Superior Cycle Stability of a Flower-Like Sb_2S_3 Anode for High-Capacity Sodium Ion Batteries. *Nanoscale* **7**, 3309–3315 (2015).
34. Hou, H. *et al*. One-Dimensional Rod-Like Sb_2S_3-Based Anode for High-Performance Sodium-Ion Batteries. *ACS Appl. Mater. Interfaces* **7**, 19362–19369 (2015).
35. Yu, D. Y. W., Hoster, H. E. & Batabyal, S. K. Bulk Antimony Sulfide with Excellent Cycle Stability as Next-Generation Anode for Lithium-Ion Batteries. *Sci. Rep.* **4**, 4562 (2014).
36. Rui, X., Tan, H. & Yan, Q. Nanostructured Metal Sulfides for Energy Storage. *Nanoscale* **6**, 9889–9924 (2014).
37. Yu D.Y.W., *et al*. High-Capacity Antimony Sulphide Nanoparticle-Decorated Graphene Composite as Anode for Sodium-Ion Batteries. *Nat Commun* **4**, (2013).
38. Prikhodchenko, P. V. *et al*. Conversion of Hydroperoxoantimonate Coated Graphenes to Sb_2S_3@Graphene for a Superior Lithium Battery Anode. *Chem. Mater.* **24**, 4750–4757 (2012).
39. Park, C.-M., Hwa, Y., Sung, N.-E. & Sohn, H.-J. Stibnite (Sb_2S_3) and Its Amorphous Composite as Dual Electrodes for Rechargeable Lithium Batteries. *J. Mater. Chem.* **20**, 1097–1102 (2010).
40. Yang, H., Su, X. & Tang, A. Microwave Synthesis of Nanocrystalline Sb_2S_3 and Its Electrochemical Properties. *Mater. Res. Bull.* **42**, 1357–1363 (2007).
41. Choi, J.-H., Ha, C.-W., Choi, H.-Y., Shin, H.-C. & Lee, S.-M. High Performance Sb_2S_3/carbon Composite with Tailored Artificial Interface as an Anode Material for Sodium Ion Batteries. *Met. Mater. Int.* **23**, 1241–1249 (2017).
42. Ge, P. *et al*. Enhanced Stability of Sodium Storage Exhibited by Carbon Coated Sb_2S_3 Hollow Spheres. *Mater. Chem. Phys.* **203**, 185–192 (2018).
43. Xie, J. *et al*. Template-Free Synthesis of Sb_2S_3 Hollow Microspheres as Anode Materials for Lithium-Ion and Sodium-Ion. *Batteries. Nano-Micro Lett.* **10**, 12 (2017).
44. Pan J., *et al*. Template-Free Synthesis of Sb_2S_3 Micro Tubes as the Anode Materials for Sodium-Ion Batteries. In: *Advanced Materials and Energy Sustainability*).
45. Yan, C. *et al*. Double Surfactant-Directed Controllable Synthesis of Sb_2S_3 Crystals with Comparable Electrochemical Performances. *CrystEngComm* **16**, 7753–7760 (2014).
46. Chen, G., Yan, L., Luo, H. & Guo, S. Nanoscale Engineering of Heterostructured Anode Materials for Boosting Lithium-Ion Storage. *Adv. Mater.* **28**, 7580–7602 (2016).
47. Oszajca, M. F., Bodnarchuk, M. I. & Kovalenko, M. V. Precisely Engineered Colloidal Nanoparticles and Nanocrystals for Li-Ion and Na-Ion Batteries: Model Systems or Practical Solutions? *Chem. Mater.* **26**, 5422–5432 (2014).
48. Yi, Z., Han, Q., Cheng, Y., Wu, Y. & Wang, L. Facile Synthesis of Symmetric Bundle-Like Sb_2S_3 Micron-Structures and Their Application in Lithium-Ion Battery Anodes. *Chem. Commun.* **52**, 7691–7694 (2016).
49. Ma, J. *et al*. Sb_2S_3 with Various Nanostructures: Controllable Synthesis, Formation Mechanism, and Electrochemical Performance toward Lithium Storage. *Chem: Eur. J.* **16**, 13210–13217 (2010).
50. Wu, Y. *et al*. Graphene Scrolls Coated Sb_2S_3 Nanowires as Anodes for Sodium and Lithium Ion. *Batteries. Nano-Struct Nano-Objects* **15**, 197–204 (2018).
51. Pan, J. *et al*. Sb_2S_3 Single Crystal Nanowires with Comparable Electrochemical Properties as an Anode for Sodium Ion. *Batteries. Surf. Interfaces* **10**, 170–175 (2018).
52. Xiao, K. *et al*. Facile Hydrothermal Synthesis of Sb_2S_3 Nanorods and Their Magnetic and Electrochemical Properties. *ECS Solid. State Lett.* **2**, P51–P54 (2013).
53. Zhou, X., Bai, L., Yan, J., He, S. & Lei, Z. Solvothermal Synthesis of Sb_2S_3/C Composite Nanorods with Excellent Li-Storage Performance. *Electrochim. Acta* **108**, 17–21 (2013).
54. Hameed, A. S., Reddy, M. V., Chen, J. L. T., Chowdari, B. V. R. & Vittal, J. J. RGO/Stibnite Nanocomposite as a Dual Anode for Lithium and Sodium Ion Batteries. *ACS Sustain. Chem. Eng.* **4**, 2479–2486 (2016).
55. Li, J. *et al*. *In Situ* Growth of Sb_2S_3 on Multiwalled Carbon Nanotubes as High-Performance Anode Materials for Sodium-Ion Batteries. *Electrochim. Acta* **228**, 436–446 (2017).
56. Wu, F., Guo, X., Li, M. & Xu, H. One-Step Hydrothermal Synthesis of Sb_2S_3/reduced Graphene Oxide Nanocomposites for High-Performance Sodium Ion Batteries Anode Materials. *Ceram. Int.* **43**, 6019–6023 (2017).
57. Hwang, S. M., Kim, J., Kim, Y. & Kim, Y. Na-Ion Storage Performance of Amorphous Sb_2S_3 Nanoparticles: Anode for Na-Ion Batteries and Seawater Flow Batteries. *J. Mater. Chem. A* **4**, 17946–17951 (2016).
58. Wang, S. *et al*. Green and Facile Fabrication of MWNTs@Sb_2S_3@PPy Coaxial Nanocables for High-Performance Na-Ion Batteries. *Part. Part Syst. Charact.* **33**, 493–499 (2016).
59. Abulikemu, M., Del Gobbo, S., Anjum, D. H., Malik, M. A. & Bakr, O. M. Colloidal Sb_2S_3 Nanocrystals: Synthesis, Characterization and Fabrication of Solid-State Semiconductor Sensitized Solar Cells. *J. Mater. Chem. A* **4**, 6809–6814 (2016).
60. Talapin, D. V. & Murray, C. B. PbSe Nanocrystal Solids for n- and p-Channel Thin Film Field-Effect Transistors. *Sci.* **310**, 86–89 (2005).
61. Oszajca, M. F. *et al*. Colloidal BiF_3 Nanocrystals: a Bottom-Up Approach to Conversion-Type Li-Ion Cathodes. *Nanoscale* **7**, 16601–16605 (2015).
62. Kravchyk, K. *et al*. Monodisperse and Inorganically Capped Sn and Sn/SnO_2 Nanocrystals for High-Performance Li-Ion Battery Anodes. *J. Am. Chem. Soc.* **135**, 4199–4202 (2013).
63. Liu, X. H. *et al*. Size-Dependent Fracture of Silicon Nanoparticles During Lithiation. *ACS Nano* **6**, 1522–1531 (2012).

Acknowledgements

This research is part of the activities of SCCER HaE, which is financially supported by Innosuisse (the Swiss Innovation Agency). This work was also financially supported by the Swiss National Science Foundation (SNF Ambizione Energy grant, Grant No. PZENP2_154287) and the Competence Center for Energy and Mobility (CCEM, Project SLIB). The authors thank Frank Krumeich for help with the EDXS measurements. The authors are grateful to the research facilities of ETH Zurich (ETH Electron Microscopy Center, Department of Chemistry and Applied Biosciences) and Empa (Empa Electron Microscopy Center and Laboratory for Mechanics of Materials & Nanostructures) for use of their instruments and technical assistance.

Author contributions

The manuscript was written through contributions of all authors. K.V.K., M.I.B. and M.V.K. designed the experimental work. M.I.B. synthesized Sb_2S_3 NPs and performed XRD, TEM, and STEM-EDXS measurements. K.V.K. conducted all electrochemical measurements reported in the paper. K.V.K. and M.V.K. wrote the paper. All authors have given approval to the final version of the manuscript.

Competing interests

The authors declare no competing interests.

Additional information

Supplementary information is available for this paper at https://doi.org/10.1038/s41598-020-59512-3.

Correspondence and requests for materials should be addressed to K.V.K. or M.I.B.

Reprints and permissions information is available at www.nature.com/reprints.

Publisher's note Springer Nature remains neutral with regard to jurisdictional claims in published maps and institutional affiliations.